Density evaluation of tungsten W24+, W25+, and W26+ ions using unresolved transition array at 27 34 A in Large Helical Device

Density evaluation of tungsten W^{24+}, W^{25+} and W^{26+} ions using unresolved transition array at 27-34 Å in Large Helical Device

Y.Liu[1], S.Morita[1,2], I.Murakami[1,2], T.Oishi[1,2], M.Goto[1,2] and X.L.Huang[2]

[1]Graduate University for Advanced Studies, Toki 509-5292, Gifu, Japan

[2]National Institute for Fusion Science, Toki 509-5292, Gifu, Japan

Abstract

Extreme ultraviolet (EUV) spectra of tungsten unresolved transition array (UTA) in 15-70 Å has been studied in Large Helical Device (LHD) by injecting a tungsten pellet. Vertical profiles of the UTA line are measured with a space-resolved EUV spectrometer. In our previous result, it has been found that the UTA line at wavelength intervals of 32.16-33.32, 30.69-31.71 and 29.47-30.47 Å is composed of a single ionization stage of W^{24+}, W^{25+} and W^{26+}, respectively. In the present report, then, density of the W^{24+}, W^{25+} and W^{26+} ions is evaluated from the radial profile measured at such specified wavelength intervals. In order to evaluate the ion density, a photon emission coefficient for the W^{24+}, W^{25+} and W^{26+} ions is calculated using a collisional-radiative (CR) model. The chord-integrated radial profile of UTA lines is converted to a local emissivity profile based on Abel inversion technique. The tungsten density profile of W^{24+}, W^{25+} and W^{26+} ions is thus obtained from the local emissivity profile and the photon emission coefficient in addition to the temperature and density profiles. A detailed analysis of the obtained profile is done for the W^{24+} ion by investigating dependences on the electron density and the number of tungsten particles injected by the pellet. A total tungsten ion density, n_W, near $\rho = 0.7$ where the W^{24+} ion locates is also estimated from the W^{24+} ion density with fractional abundance in ionization equilibrium calculated with ADAS code. The value of n_W evaluated from the present CR model seems to be large, when it is compared with n_W estimated from the number of tungsten particles injected by the pellet. Discussions are made with the n_W evaluated from the photon emission coefficient in CL version of ADAS code.

1. Introduction

ITER (International Thermonuclear Experimental Reactor) is a next-generation tokamak device for fusion research aimed at carrying out D-T burning plasma experiments, where the electron temperature of plasma is very high, e.g. 35 keV [1]. In order to improve the heat load capability and to reduce the erosion and tritium retention rates of divertor plates [2], tungsten is adopted for the divertor material of ITER instead of carbon material which has been used in tokamaks for many years [3, 4]. It is expected that a long pulse discharge with high-performance plasma can be sufficiently maintained with the tungsten divertor in ITER. On the other hand, it is well known that the tungsten ion has a large cooling rate [5] due to the line radiation loss and tends to accumulate at the plasma central region, so called impurity accumulation [6]. These phenomena easily decrease the plasma performance of ITER. In the ITER discharge, therefore, the tungsten density, n_w, has to be kept below the critical level of $n_w/n_e \sim 10^{-5}$, where n_e is the electron density [7]. It also indicates an importance of the tungsten diagnostic, in particular, measurement of the tungsten density. Until now, there are a few reports on the tungsten density analysis. A two-dimensional (2-D) tungsten density distribution is calculated with a combination of neoclassical and gyrokinetic simulation codes based on the 2-D soft x-ray (SXR) diagnostic for the tungsten transport study in JET [8] and a tungsten concentration (n_w/n_e) is obtained from the effective charge (Z_{eff}) diagnostic in ASDEX-U for the tungsten cooling rate determination [9]. However, any direct measurement of tungsten ion density from the spectroscopic diagnostic has not been reported yet.

Since the edge electron temperature of ITER plasmas is estimated to range in $0.2 \leq T_e \leq 4$ keV [10, 11], pseudo-continuum tungsten spectra called unresolved transition array (UTA) [12] emitted at extreme ultraviolet (EUV) wavelength ranges of 18-33 Å and 44-64 Å are very important for studying the edge tungsten behavior in ITER [13]. In LHD, the electron temperature of neutral-beam heated plasmas typically ranges in 1-4 keV and has a similar temperature range to the edge plasma of ITER. Then, the tungsten UTA spectrum has been extensively investigated by injecting a coaxial graphite pellet including a thin tungsten wire [14], which can easily penetrate a thick stochastic magnetic field layer [15] having the capability of enhancing the impurity screening in the plasma edge [16]. A spectral structure of the UTA has been studied by analyzing an electron temperature dependence of the UTA line intensity at each wavelength interval and measuring the peak position of radial profiles of the UTA line. As a result, it has been found that the tungsten UTA line at wavelength intervals of 32.16-33.32 Å, 30.69-31.71 Å and 29.47-30.47 Å is composed of a single ionization stage of W^{24+}, W^{25+} and W^{26+}, respectively [17].

In the present study, the tungsten ion density is evaluated as the first attempt based on the previous study on the tungsten UTA line. At first, a vertical intensity profile of the UTA line is measured with a space-resolved EUV spectrometer in LHD for the W^{24+}, W^{25+} and W^{26+} ions at wavelength intervals mentioned above. A local emissivity profile is reconstructed from the intensity profile using Abel inversion method [18]. Next, a photon emission coefficient is calculated with a collisional-radiative (CR) model developed for the UTA spectrum analysis in which two effects of inner-shell excitation and configuration interaction are newly considered [19]. The tungsten ion density can be thus evaluated from the local emissivity profile and photon emission coefficient in addition to the electron temperature and density profiles measured with high accuracy. A total tungsten density is also estimated from the analyzed

W^{24+} ion density profile in the vicinity of $\rho = 0.7$ based on the fractional abundance in ionization equilibrium calculated with ADAS code [20].

2. Experimental setup

A space-resolved EUV spectrometer, EUV_Short2 [21], is installed on #10-O port of LHD for measuring a spatial distribution of impurity line emissions in the wavelength range of 10-130 Å. A schematic diagram of the spectrometer arrangement with horizontal dispersion is shown in Fig. 1. The optical axis of EUV spectrometer is perpendicular to the toroidal magnetic field of LHD. A narrow horizontal slit with vertical width of 1.0 mm is placed in front of the entrance slit for the spatial resolution along vertical direction and a back-illuminated charge-coupled device (CCD: 1024 × 255 pixels, 26.6 × 6.6 mm^2, 26 × 26 μm^2/pixel) detector is used for recording the two-dimensional image, i.e., wavelength vs vertical line intensity distribution. The spectrometer placed at 9.457 m away from the plasma center at the magnetic axis of $R_{ax} = 3.6$ m has the capability of measuring a wide vertical range of 0.5 m, which corresponds to a half diameter at the short axis of an elliptical LHD plasma. A sub-image mode with 204 × 127 channels is usually used for a routine measurement by summing up five adjacent pixels at long axis and two adjacent pixels at short axis of the CCD. A space-resolved spectrum of impurity line emissions is thus obtained with sampling time of 100 ms. The spectral intensity is absolutely calibrated with high accuracy by comparing two bremsstrahlung continuum profiles between EUV and visible ranges [22]. In the present study, the vertical observation range of EUV_Short2 is fixed to the upper half ($0 \le Z \le 0.5$ m) of LHD plasma at horizontally elongated plasma cross section.

A grazing-incidence EUV spectrometer called EUV_Short [23] is also used to observe tungsten spectra in the wavelength range of 10-130 Å. In the present study, a relatively narrow entrance slit of 30 μm width is adopted to obtain a good spectral resolution because the angle of incidence of the spectrometer is very large, i.e., 88.6°. The wavelength spectrum is sequentially obtained at every 5 ms interval in a full-binning mode of CCD.

3. Experimental results

A. Typical discharge with tungsten pellet injection

A series of experiments with tungsten pellet injection have been carried out in LHD for tungsten spectroscopy. A typical discharge with a coaxial tungsten pellet (tungsten wire: 0.05 mm in diameter × 1.0 mm in length, graphite cylinder: 0.7 mm in diameter × 0.7 mm in length) injected at horizontal mid-plane is shown in Fig. 2. The discharge is sufficiently maintained by three negative-ion-source-based neutral beams (n-NBI#1, #2 and #3) with energy of 180 keV during 3.6-6.2 s. A tungsten pellet with a relatively large amount of tungsten is injected at t = 4.3 s. The number of particles injected by the pellet is $N_C = 2.7 \times 10^{19}$ for carbon and $N_W = 1.2 \times 10^{17}$ for tungsten. If the carbon and tungsten ions are uniformly distributed in the whole LHD plasma volume of 30 m^3, we obtain a local density of $n_C = 8.9 \times 10^{11}$ cm^{-3} for carbon and $n_W = 4.1 \times 10^9$ cm^{-3} for tungsten. Therefore, the small density rise at t = 4.3 s just after pellet injection, i.e. $\Delta n_e = 0.6 \times 10^{13}$ cm^{-3}, is brought by the carbon ions because the density rise from tungsten ions is negligibly small. If we assume that all carbon ions from the pellet are ionized to C^{6+},

the density rise from carbon $\Delta n_e(C)$, is 0.53×10^{13} cm^{-3} (= $n_C \times 6$), of which the value shows a good agreement with Δn_e. However, the continuous density increase from $n_e = 3.6 \times 10^{13}$ cm^{-3} at t = 4.3 s to 5.6×10^{13} cm^{-3} at t = 6.3 s, i.e. $\Delta n_e = 2.0 \times 10^{13}$ cm^{-3}, seen in Fig. 2(b), does not originate in the pellet injection. In LHD, a stochastic magnetic field layer exists outside the core plasma [24]. It is well known that the upstream flow of impurity ions from divertor to core plasma through the stochastic magnetic field layer is perturbed and changed to the downstream flow by the stochastic magnetic field layer, so called impurity screening [16]. Hydrogen ions are also screened by the stochastic magnetic field layer. When the tungsten pellet is injected, the plasma size becomes a little smaller, and the edge plasma at outer region in the stochastic magnetic field layer is vanished by a large radiation loss of the tungsten ions. After the tungsten pellet injection, then, the impurity screening effect is weakened and resultantly more ions are transferred to the core plasma. Therefore, the continuous density increase originates in the weakened effect of edge particle screening based on a reduction of the edge temperature by the tungsten radiation loss [16]. The central electron temperature, T_{e0}, after the pellet injection gradually decreases reflecting increases in the total radiation power, P_{rad}, and the electron density. The UTA line intensity from W^{24+} (32.16-33.32 Å), W^{25+} (30.69-31.71 Å) and W^{26+} (29.36 -30.47 Å) ions are plotted in Figs. 2(f), (g) and (h), respectively. It is noticed that the UTA line from W^{26+}, W^{25+} and W^{24+} ions reach the peak intensity in sequence, i.e., t = 5.3, 5.4 and 5.6 s. Since the electron temperature continuously decreases, the ionization stage of tungsten ions in the plasma center is gradually lowered as a function of time.

The electron temperature and density profiles during t = 4.2-6.2 s are shown in Figs. 3(a) and 3(b), respectively. The horizontal axis means a normalized plasma radius, i.e., $\rho = 0$ at plasma center and $\rho = 1.0$ at LCFS (last closed flux surface). A steep electron temperature profile at t = 4.2 s before the pellet injection gradually changes to a flatter profile after the pellet injection due to the enhanced radiation loss and increased electron density. On the contrary, the electron density profile does not change so much before and after the pellet injection, while the density itself continuously increases during the n-NBI phase.

The tungsten spectrum in the wavelength range of 18-36 Å is measured with EUV_Short spectrometer at $\Delta t = 0.9$ s after the pellet injection, as shown in Fig. 4. The ionization stage of UTA lines in each peak group is estimated by referring the previous work from CoBIT [25] and plasma device [12]. As shown in the figure, the tungsten UTA spectrum is composed of many ionization stages of tungsten ions, e.g. from W^{24+} to W^{33+} in the present spectrum. These UTA lines are basically formed by four transitions of 6g-4f, 5g-4f, 5f-4d and 5g-4f. In our previous work [17], the UTA line at wavelength intervals of 27.20-27.62 Å, 28.38-28.70 Å, 29.36-30.47 Å, 30.69-31.71 Å and 32.16-33.32 Å indicated with hatched regions is found to be composed of a single ionization stage of W^{28+}, W^{27+}, W^{26+}, W^{25+} and W^{24+}, respectively. In the present study, three UTA lines at 29.36-30.47 Å, 30.69-31.71 Å and 32.16-33.32 Å measured with EUV_Short2 are used to evaluate the tungsten density profiles of W^{26+}, W^{25+} and W^{24+} ions, respectively, since such wavelength intervals are relatively wider, resulting in sufficient signal counts and better profile measurement. A good-quality profile of impurity line emissions is absolutely necessary for obtaining the local emissivity profile using Abel inversion method to reduce the uncertainty. Details on the Abel inversion are described later.

B. Calculation of photon emission coefficients

The fractional abundance of W^{22+}-W^{34+} ions in ionization equilibrium is calculated at $n_e = 4 \times 10^{13}$ cm^{-3} using ADAS code, as shown in Fig. 5(a). Since the ionization energy of tungsten ion becomes large with the ionization stage, the electron temperature range where a certain tungsten ion exists also becomes wide with the ionization stage. Three sequential tungsten ions of the W^{24+}, W^{25+} and W^{26+} having a relatively narrow electron temperature window take the maximum abundance at similar temperatures of 0.64, 0.77 and 0.93 keV, respectively. In the toroidal plasma, then, the radial positions where the three tungsten ions exist are close to each other, when the electron temperature is sufficiently high (see Fig. 3(a)).

Total photon emission coefficients of W^{24+}, W^{25+} and W^{26+} at wavelength intervals of 32.16-33.32, 30.69-31.71 and 29.47-30.47 Å are calculated with CR model developed for analysis of the tungsten UTA spectrum [19]. In the CR model, principal quantum number up to n = 7 and 11753, 13772 and 7515 J-resolved fine-structure levels are taken into account for W^{24+}, W^{25+} and W^{26+} ions, respectively, and 19-27 electron configurations are considered for one ion. Effects of inner-shell excitation and configuration interaction are also considered in addition to general atomic processes. The photo emission coefficient at each wavelength interval then includes a lot of transitions. In practice, there are more than 100 thousands emission lines at each wavelength interval.

The result of the modeling is plotted in Fig. 5(b). The total photon emission coefficient, f_{PEC}, of W^{26+} (dotted line) is clearly larger than that of W^{24+} (solid line) and W^{25+} (dashed line). The emission coefficient is approximately constant at $T_e \geq 0.8$ keV, while it is greatly sensitive to the electron temperature at $T_e \leq 0.4$ keV. In the toroidal plasma, however, such tungsten ions always stay at a fixed narrow temperature window because the electron temperature largely changes along the plasma radial direction (see Fig. 3(a)). Therefore, the emission intensity is not so sensitive to the central electron temperature, if the central electron temperature is not so low that the tungsten ions stay at the plasma center. As the central electron temperature after the tungsten pellet injection is maintained above 1 keV, the W^{24+}-W^{26+} ions always exist in the plasma during the whole n-NBI phase (see Figs. 2 and 3(a)).

In Fig. 5(c), the photon emission coefficient of W^{24+}, W^{25+} and W^{26+} at 32.16-33.32, 30.69-31.71 and 29.47-30.47 Å is calculated with ADAS code (CL version, e.g. data file “arf40_cl#w24.dat”). In this version, 28-29 electron configurations are considered, while an energy level splitting among sublevels is not taken into consideration. The photon emission coefficient of the W^{24+} ion obtained from ADAS code is three times larger than that from the present CR model. A cascade process from higher excited levels may enhance the photon emission coefficient in the ADAS code calculation. The photon emission coefficient of the W^{26+} ion is considerably different from other two coefficients. In the ADAS calculation the number of tungsten lines is only one for the W^{24+} ion at 32.16-33.32 Å, while it is two for the W^{25+} and W^{26+} ions at 30.69-31.71 and 29.47-30.47 Å, respectively.

The photon emission coefficients of W^{24+}-W^{26+} at wavelength intervals of 32.16-33.32, 30.69-31.71 and 29.47-30.47 Å from the present CR model are replotted as a function of normalized plasma radius in Fig. 6 with solid, dashed and dotted lines, respectively The plot is done for the electron temperature profile at t = 4.7 s in Fig. 2. It is clear that the value of f_{PEC} is not so sensitive to T_e, at least, at $\rho \leq 0.85$.

C. Error estimation in local emissivity profile analysis

Abel inversion method [18] is usually applied to reconstruct the local emissivity profile from the measured profile of spectral line intensity, which is integrated along an observation chord, based on an assumption that the local emissivity is uniform at the same magnetic surface, as shown in Fig. 1, like an onion cross. Because the temperature and density in toroidal plasmas are basically constant at all poloidal positions on the magnetic surface. In LHD, it has been experimentally verified that the intensity of line emissions from tungsten ions behaves as a function of the magnetic surface and any up-down asymmetry has not been observed in the tungsten spectrum [26]. Then, the magnetic surface necessary for the reconstruction is calculated with the three-dimensional equilibrium code, Variational Moments Equilibrium Code (VMEC) [27]. The local emissivity profile is expressed by the following matrix:

$$\varepsilon(\rho) = L^{-1}I(Z), \quad (1)$$

where $\varepsilon(\rho)$, L and I(Z) are the local emissivity profile [photons·cm^{-3}·s^{-1}], a matrix of chord length [cm] and the vertical intensity profile [photons·cm^{-2}·s^{-1}], respectively. There are many intersections between a single observation chord and many different magnetic surfaces shown in Fig. 1. A unit chord length between two adjacent magnetic surfaces is calculated as a function of ρ for each observation chord. Then, the unit chord lengths as a function of ρ calculated for a single observation chord form a matrix, L, against all observation chords as a function of Z.

At the first step of Abel inversion, an appropriate set of magnetic surfaces is determined with the VMEC calculation so that the electron temperature profile along major plasma radius can be symmetric against a derived normalized radius, ρ, between outer and inner plasma radii, because the magnetic surface is distorted by the presence of plasmas, and the magnetic axis is outwardly shifted as a function of the pressure profile and beta value. Here, the beta value means a ratio of the plasma pressure to the magnetic field pressure, i.e. $P/(B^2/2\mu_0)$, where B and μ_0 are the magnetic field strength and the permeability in vacuum, respectively. The beta value is generally obtained from the diamagnetic flux measurement as a volume-averaged beta value because the diamagnetic flux indicates the total plasma stored energy. The most appropriate magnetic surface structure is then determined by adjusting the measured pressure profile and beta value.

It is important to estimate the uncertainty in the local emissivity profile calculated with Abel inversion method [28] in evaluating the tungsten ion density. Figures 7(a), (b) and (c) show an example of the vertical intensity of W^{24+} emission at 32.16-33.32 Å, the chord length of sight lines and the local W^{24+} emissivity, respectively. The vertical position in the vertical intensity profile of Fig. 7(a) is also converted into the normalized radius at plasma axis of R_{ax} = 3.6 m. Here, the pressure profile of $P(\rho) = P_0(1-\rho^8)(1-\rho^2)$ [29-31], which is expressed by '(8020)', is used for the calculation with volume-averaged beta of 0.44%, where P_0 is the central plasma pressure. In LHD, the pressure profile of (8020) is generally used as the standard value for the profile analysis [31]. In addition, the magnetic surface at $\rho > 1.0$ outside LCFS is assumed in a usual way, i.e., a simple expansion of the magnetic surface contour at $\rho = 1.0$.

The uncertainty of the intensity profile, I(0.44%_8020), in Fig. 7(a) analyzed with β = 0.44% and pressure profile of (8020) is estimated by comparison with an intensity profile, I(β_P), analyzed with different β value and pressure profile. Then, the uncertainty is obtained by

$$(I(\beta\_P) - I(0.44\%\_8020)) / I(0.44\%\_8020) = I_{error} / I(0.44\%\_8020), \quad (2)$$

where, I_{error} is defined as a difference between two intensity profiles at β = 0.44% (8020) in Fig. 7(a) and at other magnetic surface structures with different β value and pressure profile. The result is shown in Fig. 7(d). From the figure, it is found that the uncertainty is larger at a radial location where the intensity rapidly changes. It is also found that the value of I_{error} / I has a different sign at different β values with the same pressure profile of (8020) and at different pressure profiles with similar β values. It indicates the present choice, i.e., β = 0.44% and (8020) pressure profile, is adequate for analyzing the profile.

The definition in the uncertainty estimation of chord length, L, and local emissivity profile is also the same as the intensity profile, of which the result is shown in Figs. 7(e) and 7(f), respectively. The value of L_{error} / L_{chord} in Fig. 7(e) shows a relatively small difference in the whole radial location for all the cases with different β values and pressure profiles. It means the L_{chord} does not bring any significant effect on the local emissivity profile. On the contrary, the value of ε_{error} / ε in Fig. 7(f) has a large error in the vicinity of plasma center except for the case of β = 0.55% and (8020) pressure profile. It strongly suggests the choice of an adequate magnetic surface structure is extremely important for reducing the uncertainty in analyzing the local emissivity profile. Thus, the uncertainty in the local emissivity profile analyzed from the measured intensity profile can be estimated to be ±17% as the maximum value in the vicinity of $0.5 \le \rho \le 1.0$ where the W^{24+} ion exists. In addition, the uncertainty of the intensity calibration of EUV_Short2 is estimated to be 6.4% [21].

D. Evaluation of W^{24+}-W^{26+} ion density profiles

The vertical intensity profile of UTA lines at 32.16-33.32 Å from the W^{24+} ion, which is measured with EUV_Short2 spectrometer, is plotted in Fig. 8(a) for three different central electron temperatures of T_{e0} = 2.19 (dashed line), 1.95 (solid line) and 1.82 keV (dotted line) at t = 4.6 s, 4.8 s and 4.9 s, respectively. As a function of time the peak intensity near Z = 0.32 m decreases and the peak position moves inside toward the plasma center. The local emissivity profile reconstructed from the vertical intensity profile is shown in Fig. 8(b). Dependence of the peak position in the local emissivity profile on the electron temperature is clearly seen in the figure.

Based on the local emissivity profile, the density profile of W^{24+} ions, $n_{W^{24+}}(\rho)$, can be then calculated by an equation of

$$n_{W^{24+}}(\rho) = \varepsilon(\rho) / (n_e(\rho) \times f_{PEC}(T_e, n_e)), \quad (3)$$

where $n_e(\rho)$ is the electron density profile, and $f_{PEC}(T_e, n_e)$ is calculated with the present CR model shown in Fig. 5(b). The W^{24+} ion density profiles analyzed at T_{e0} = 2.19 (dashed line), 1.95 (solid line) and 1.82

keV (dotted line), which are the same as the case of Fig .8, are shown in Fig. 9(a). The W^{24+} ion density distributes in range of 3-5 × 10^9 cm^{-3}. The density profile of W^{24+} ions is also analyzed using $f_{PEC}(T_e, n_e)$ from ADAS code shown in Fig. 5(c). The result is plotted in Fig. 9(b). It is obvious that the W^{24+} ion density in Fig. 9(a) is roughly three times larger than that in Fig. 9(b), reflecting the difference in the photon emission coefficient.

In Fig. 9(c), the electron temperature where the vertical intensity profile of W^{24+} (32.16-33.32 Å), W^{25+} (30.69-31.71 Å) and W^{26+} (29.47-30.47 Å) takes the maximum value is plotted against the peak position in the vertical intensity profile. The data point in the figure is taken at 4.5-5.1 s in Fig. 2. As shown in Fig. 3(a), the electron temperature profile changes as a function of time. Meanwhile, the vertical profiles of W^{24+} (32.16-33.32 Å), W^{25+} (30.69-31.71 Å) and W^{26+} (29.47-30.47 Å) also change as a function of time. The peak in the vertical profile means the position where the tungsten ions exist. From Fig. 9(c), we can find the electron temperatures where W^{24+}, W^{25+} and W^{26+} ions exist are unchanged, even if the central electron temperature changes. It means the radial position of such tungsten ions is mainly determined by the temperature, not by the impurity transport. This fact reduces the uncertainty due to the temperature dependence of the photon emission coefficient.

Based on the analyzed W^{24+} ion density profile, the total tungsten density, $n_w(\rho)$, is estimated from an equation of

$$n_w(\rho) = n_{w^{24+}}(\rho) / f_{ab}(T_e, n_e), \qquad (4)$$

where $f_{ab}(T_e, n_e)$ is the fractional abundance of W^{24+} shown in Fig. 5(a). Here, the total tungsten density is estimated only from the peak value of W^{24+} ion profile in the vicinity of $\rho = 0.7$. The result is shown in Fig. 10 for the f_{PEC} from the present CR model (solid line) and ADAS code (dashed line). Only the peak value of W^{24+} fractional abundance in Fig. 5(a), i.e., $f_{ab}(T_e, n_e) = 0.25$ at $T_e = 0.64$ keV, is used in the estimation. It is shown in the figure that the total tungsten density continuously decreases after the tungsten pellet injection (t = 4.3 s), while the reduction becomes slower as a function of time.

From the profile measurement of EUV line emissions in several tungsten ionization stages, the tungsten ion slowly expands in the radial direction toward the plasma center. The result in Fig. 10 indicates such an expansion process. In the present case the tungsten ion almost completes the expansion at $\Delta t = 0.5$ s after the pellet injection, i.e., t = 4.8 s in Fig. 10. If all the tungsten ions are uniformly distributed in the LHD plasma, we obtain $n_W = 4.1 \times 10^9$ cm^{-3} from the number of tungsten particles injected by the pellet. The n_W from f_{PEC} with the present CR model is 3.6 times larger than the n_W estimated from the pellet size. If it is compared with n_W based on f_{PEC} from ADAS code, the n_W from ADAS code is 1.2 times larger than the n_W from the pellet size. At present, however, it is difficult to discuss on the accuracy in the f_{PEC} because another model in the ADAS code has entirely different values for the f_{PEC} due to different number of electron configurations in the model. In addition, the present CR model includes possible all atomic processes and J-resolved levels, while the dielectric recombination is not included. We need further efforts for quantitatively and accurately understanding the UTA line intensity.

The tungsten ion density profile of W^{24+}, W^{25+} and W^{26+} ions is analyzed at t = 4.7 s, as shown in Fig.

11(b) with dashed, solid and dotted lines, respectively. The electron density and temperature used for the analysis are also shown in Fig. 11(a). It is found that the peak density in the W^{26+} ion density profile is clearly smaller than those in the W^{24+} and W^{25+} ion density profiles. Since the W^{26+} ion abundance has a wider distribution against the electron temperature compared to the W^{24+} and W^{25+} ions, more ionization stages of tungsten ions exist at the temperature range of the W^{26+} ion. Then, the total tungsten density is calculated from the three density profiles in Fig. 11(b) using f_{PEC} from the present CR model. The values of n_W are reasonably similar to each other in the vicinity of $\rho = 0.7$, i.e., $n_W = (1.7 \pm 0.2) \times 10^{10}$ cm^{-3} from W^{24+}, $n_W = (1.8 \pm 0.2) \times 10^{10}$ cm^{-3} from W^{25+} and $n_W = (1.4 \pm 0.2) \times 10^{10}$ cm^{-3} from W^{26+}. It indicates that the coefficient of f_{PEC} from the present CR model is sufficiently accurate in the relative value among three wavelength intervals of the UTA line.

4. Discussions on the tungsten ion density

In order to examine the electron density dependence of W^{24+} ion density, the tungsten pellet (tungsten wire size: 0.06 mm$^{\phi}$ × 1.0 mm^{L}) has been injected in NBI discharges at different densities of 2.5, 3.2 and 4.7 × 10^{13} cm^{-3}. The number of particles included in the pellet is $N_W = 1.7 \times 10^{17}$ for tungsten. The electron temperature profile at $\Delta t = 0.1$ s after the pellet injection is plotted in Fig. 12(a). The central electron temperature decreases from 2 keV to 1 keV when the density increases. The W^{24+} ion density profile analyzed for the three density cases in the same way as before is plotted in Fig. 12(b). The W^{24+} ion density in the discharge with $n_e = 4.7 \times 10^{13}$ cm^{-3} is clearly smaller than that in lower density discharges because the tungsten density decay after the pellet injection is faster in higher density discharges. The peak value of W^{24+} ion density profiles gradually decreases due to the finite confinement time as a function of discharge time after the tungsten pellet injection. Then, a decay rate of the W^{24+} ion density can be obtained from the temporal behavior. The value is 9×10^{9} cm^{-3}/s at $n_e = 2.5 \times 10^{13}$ cm^{-3}, 15×10^{9} cm^{-3}/s at $n_e = 3.2 \times 10^{13}$ cm^{-3} and 24×10^{9} cm^{-3}/s at $n_e = 4.7 \times 10^{13}$ cm^{-3}.

The tungsten pellet with different tungsten wire sizes of 0.03 mm$^{\phi}$ × 1.0 mm^{L}, 0.05 mm$^{\phi}$ × 1.0 mm^{L} and 0.06 mm$^{\phi}$ × 1.0 mm^{L} has been also injected in NBI discharges with $n_e = 2.2$, 3.0 and 3.2 × 10^{13} cm^{-3}, respectively. The central electron temperature before the pellet injection has a similar value of 2.6 keV for three discharges. The electron temperature profile at $\Delta t = 0.1$ s after the pellet injection is shown in Fig. 13(a). The electron temperature at the small pellet (0.03 mm$^{\phi}$) injection is obviously lower than that at large pellets (0.05 mm$^{\phi}$ and 0.06 mm$^{\phi}$). Since the speed of a tungsten pellet injected with the same pressurized He gas is higher at smaller tungsten wire size, such a high-speed pellet is radially deposited at deeper position [14]. The tungsten ionization from the pellet cloud then becomes quicker because the electron temperature is high at the pellet evaporation and resultantly the radiation from tungsten ions rapidly increases in the smaller tungsten pellet.

The W^{24+} ion density profile analyzed at $\Delta t = 0.1$ s for three cases is shown in Fig. 13(b). The peak position of the W^{24+} ion density profile locates in a similar radial location near $\rho \sim 0.8$ because the target discharge is almost identical for the three cases. The tungsten W^{24+} ion density changes according to the tungsten wire size. Here, we evaluate a ratio of the total tungsten density to the injected number of

tungsten particles, n_W / N_W. The ratio is 2.4×10^{-7} cm^{-3} for 0.03 mm^{ϕ}, 2.2×10^{-7} cm^{-3} for 0.05 mm^{ϕ} and 2.0×10^{-7} cm^{-3} for 0.06 mm^{ϕ}. It is our understanding that all the ratios have similar values. Therefore, it indicates all injected tungsten particles are fairly well confined in the plasma after the ablation of the tungsten pellet.

5. Summary

A series of experiments on tungsten spectroscopy are conducted in LHD by injecting a tungsten pellet to attempt an evaluation of a tungsten ion density. The fractional abundance of W^{22+}-W^{34+} ions is calculated with ADAS code and a photon emission coefficient for W^{24+} , W^{25+} and W^{26+} ions at wavelength intervals of 32.16-33.32, 30.69-31.71 and 29.47-30.47 Å is calculated with CR model which is developed for the analysis of UTA spectra. Uncertainty in a local emissivity profile of the W^{24+} ion at 32.16-33.32 Å is evaluated with magnetic surface structures which are deformed as a function of a plasma pressure profile. The result indicates the importance of the use of an adequate magnetic surface to reduce the uncertainty.

The W^{24+} ion density is then evaluated from electron density and temperature profiles, the local emissivity profile and the photon emission coefficient. The error of W^{24+} density is evaluated from the errors of the local emissivity profile, electron density and photon emission coefficients. Then, the total tungsten density in the vicinity of $\rho = 0.7$ is calculated from a peak value of the W^{24+} ion density profile based on the fractional abundance at an electron temperature at which the W^{24+} abundance takes the maximum value. The tungsten density calculated with the photon emission coefficient from the present CR model is roughly four times larger than the tungsten density estimated from the pellet size, while the density calculated from a CL version of ADAS code is considerably closer to the density from the pellet size, i.e., within two times. However, the present result does not indicate inaccuracy in the present CR model because it includes possible all the atomic processes and a huge number of J-resolved sublevels, while it does not include dielectronic recombination. We need further efforts to qualitatively understand the UTA spectrum in both fields of experiment and modeling.

Acknowledgments

The authors thank all the members of the LHD experiment group for their cooperation including technical support. This work was partly carried out under the LHD project financial support (NIFS17ULPP010) and also partly supported by Grant-in-Aid for Scientific Research (B) No. 16H04088 and 16H04623.

References

[1] ITER Physics Basis Editors et al., Nucl. Fusion 39, 2137 (1999).

[2] C.S. Pitcher and P.C. Stangeby, Plasma Phys. Control. Fusion 39, 779 (1997).

[3] G.F. Matthews, P. Edwards, T. Hirai et al., Phys. Scr. **T128**, 137 (2007).

[4] R.A. Pitts, A. Kukushkin, A. Loarte, et al., Phys. Scr. **T13**8, 014001 (2009).

[5] D.E. Post et al., At. Data Nucl. Data Tables 20, 397 (1977).

[6] M.Z. Tokar et al., Nucl. Fusion 37, 1691 (1997).

[7] R. Neu, R.Dux, A. Geier et al., Fusion Eng. Des. **65**, 367 (2003).

[8] C. Angioni et al., Nucl. Fusion 54, 083028 (2014).

[9] T. Pütterich et al., Nucl. Fusion 50, 025012 (2010).

[10] E.J. Doyle, W.A. Houlberg, Y. Kamada et al., Nucl. Fusion **47**, S18 (2007).

[11] A.W. Leonard, A. Hermannb, K. Itamic et al., J. Nucl. Mater. **266**, 109 (1999).

[12] S. Morita, C.F. Dong, M. Goto et al., AIP Conf. Proc. 1545, 143 (2013).

[13] Y. Liu et al., Plasma Fusion Res. 13, 3402020 (2018).

[14] X.L. Huang, S. Morita, T. Oishi, M. Goto and H.M. Zhang, Rev. Sci. Instrum. **85**, 11E818 (2014).

[15] T. Morisaki, S. Sakakibara, K.Y. Watanabe, et al., Contrib. Plasma Phys. 40, 266 (2000).

[16] S. Morita, C.F. Dong, M. Kobayashi et al., Nucl. Fusion **53**, 093017 (2013).

[17] Y. Liu, S. Morita, X.L. Huang, T. Oishi, M. Goto and H.M. Zhang, J. Appl. Phys. **122**, 233301 (2017).

[18] L.M. Smith, D.R. Keefer and S.I. Sudharsanan, J. Quant. Spectrosc. Radiat. Transfer 39, 367 (1988).

[19] I. Murakami, H.A. Sakaue, C. Suzuki, et al., Nucl. Fusion **55**, 093016 (2015).

[20] H.P. Summers, The ADAS User Manual, version 2.6 http://www.adas.ac.uk (2004).

[21] X.L. Huang, S. Morita, T. Oishi, M. Goto, and C.F. Dong, Rev. Sci. Instrum. **85**, 043511 (2014).

[22] C.F. Dong, S. Morita, M. Goto and E.H. Wang, Rev. Sci. Instrum. **82**, 113102 (2011).

[23] M.B. Chowdhuri, S. Morita and M. Goto, Appl. Opt. **47**, 135-146 (2008).

[24] S. Morita, E.H. Wang, M. Kobayashi et al., Plasma Phys. Control. Fusion 56, 094007 (2014).

[25] H.A. Sakaue, D. Kato, N. Yamamoto, N. Nakamura and I. Murakami, Phys. Rev. A **92**, 012504 (2015).

[26] Y. Liu, S. Morita, X.L. Huang, T. Oishi, M. Goto and H.M. Zhang, Rev. Sci. Instrum. **87**, 11E308 (2016).

[27] S.P. Hirshman, W.I. van Rij and P. Merkel, Comput. Phys. Commun. **43**, 143 (1986).

[28] H.Y. Zhou, S. Morita, M. Goto and C.F. Dong, J. Appl. Phys. 107, 053306 (2010).

[29] Y. Suzuki, N. Nakajima, K. Watanabe, Y. Nakamura and T. Hayashi, Nucl. Fusion 46, L19-L24 (2006).

[30] N. Nakajima, S.R. Hudson, C.C. Hegna and Y. Nakamura, Nucl. Fusion 46, 177-199 (2006).

[31] S. Sakakibara, K.Y. Watanabe et al., Nucl. Fusion 55, 083020 (2015).

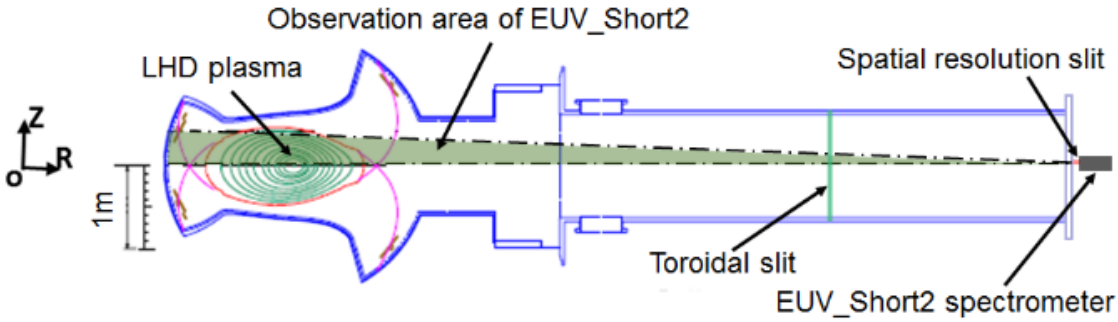

Fig. 1. Side view of space-resolved EUV_Short2 spectrometer.

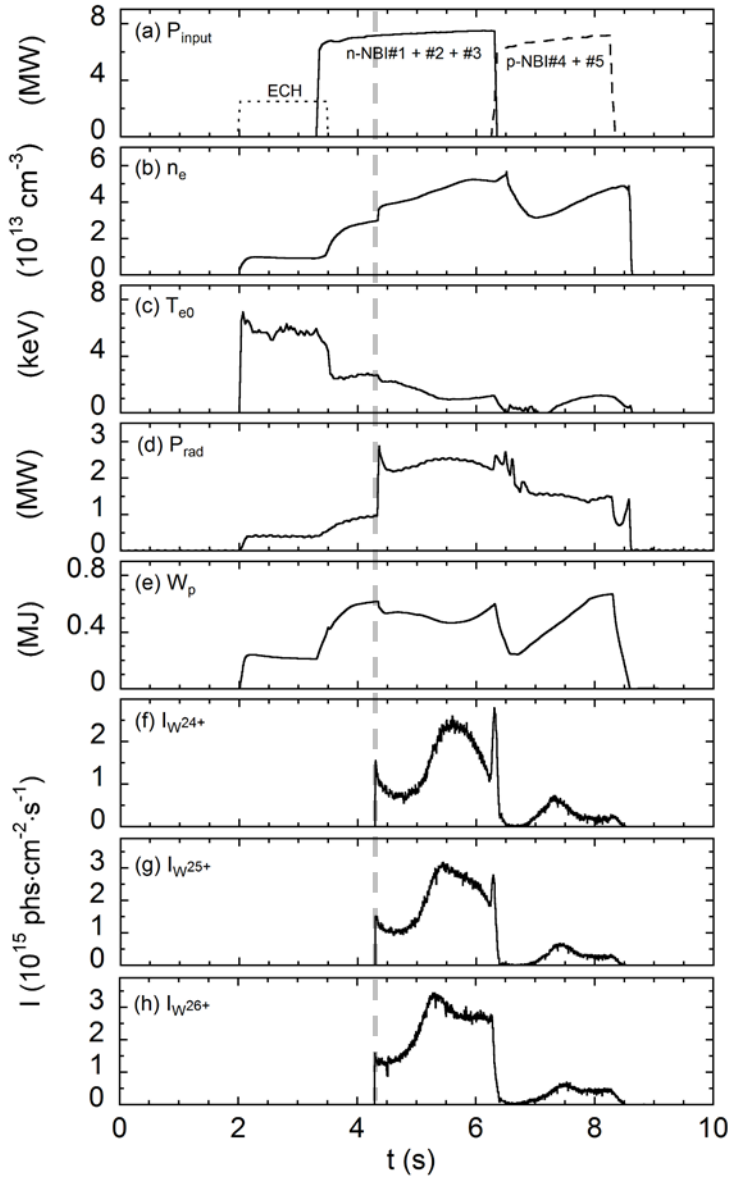

Fig. 2. Discharge waveform with tungsten pellet injected at 4.3 s; (a) NBI input power, (b) line-averaged electron density, (c) central electron temperature, (d) total radiation power, (e) plasma stored energy, (f) emission intensity from W^{24+} ions at wavelength interval of 32.18-33.34 Å, (g) intensity of W^{25+} emission line at wavelength interval of 30.69-31.71 Å, and (h) intensity of W^{26+} emission line at wavelength interval of 29.36-30.47 Å. A coaxial graphite pellet (0.7 mm^{ϕ} × 0.7 mm^{L}) with a tungsten wire size of 0.05 mm^{ϕ} × 1.0 mm^{L} is injected at t = 4.3 s of which the timing is indicated with vertical dashed line.

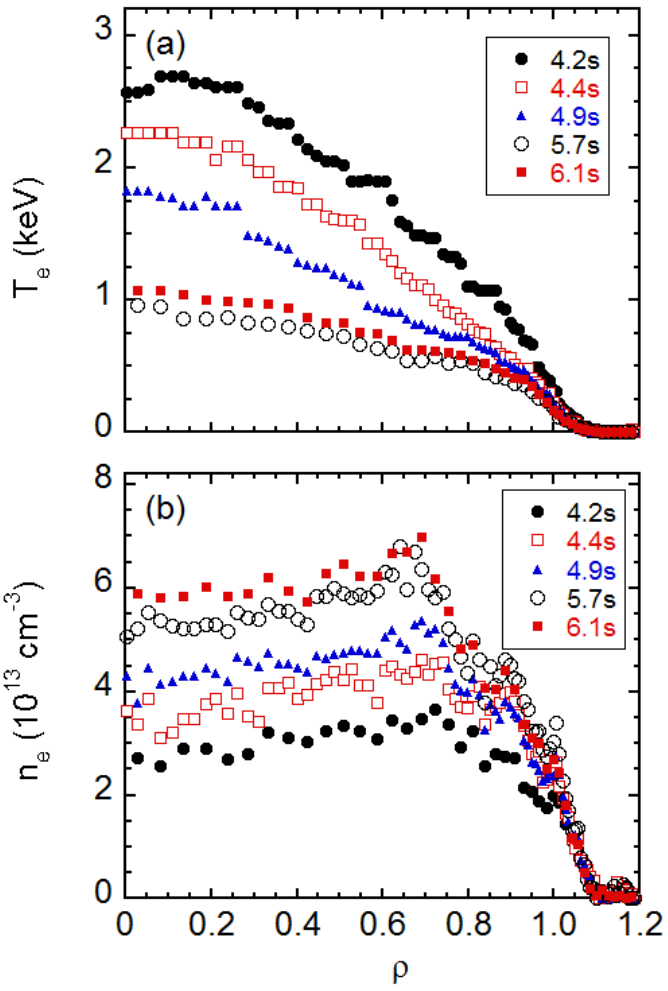

Fig. 3. (a) Electron temperature and (b) density profiles at t = 4.2 (just before pellet injection), 4.4 (just after pellet injection), 4.9, 5.7 and 6.1 s.

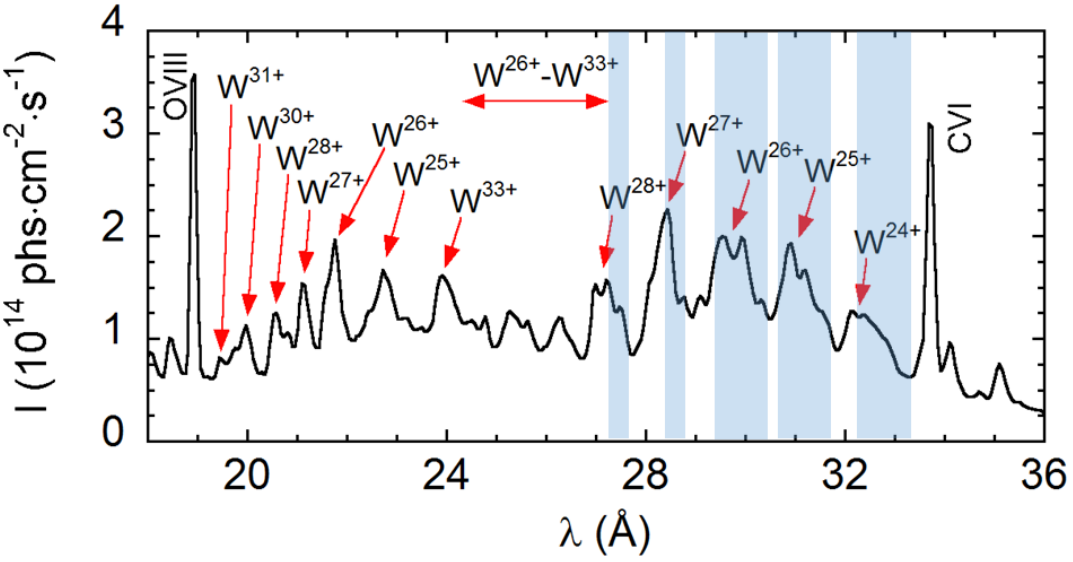

Fig. 4. Tungsten UTA spectrum at wavelength range of 18-36 Å measured by EUV_Short. Shaded area indicates a wavelength interval in which UTA emission lines are composed of a single ionization stage.

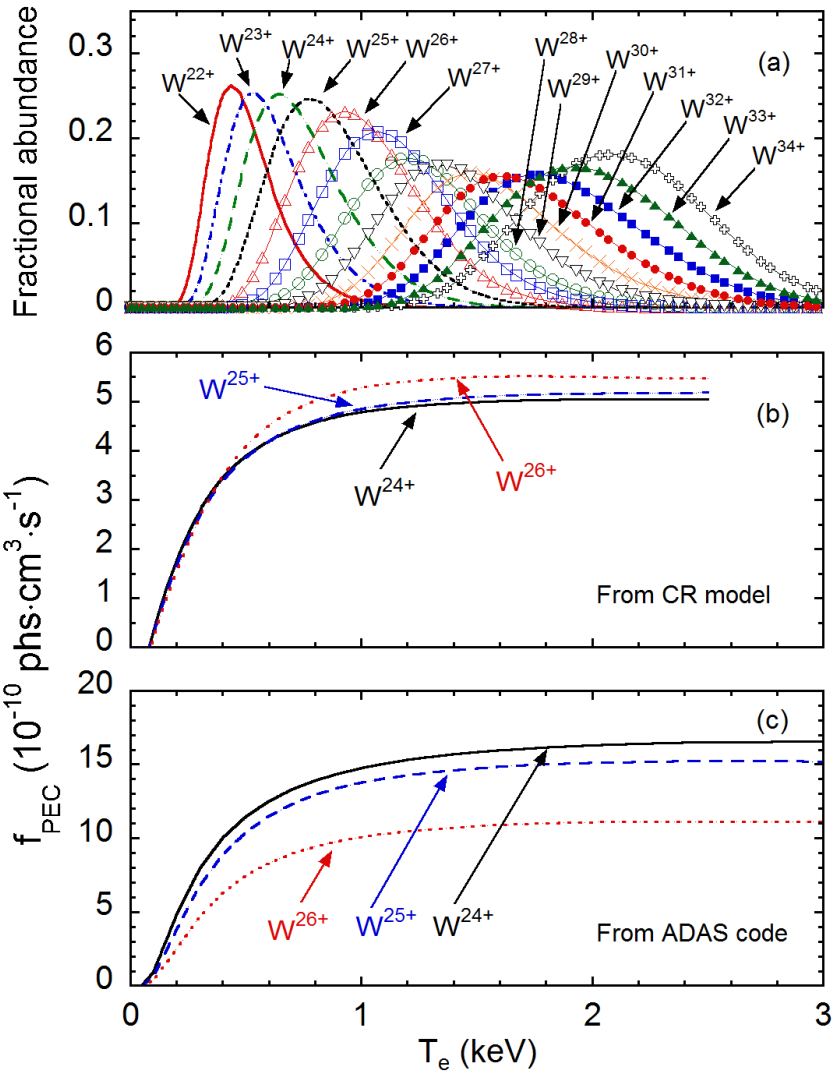

Fig. 5. (a) Fractional abundance of W^{22+}-W^{34+} calculated with ADAS code at $n_e = 4 \times 10^{13}$ cm^{-3}, and total photon emission coefficient of W^{24+} (32.16-33.32 Å: solid line), W^{25+} (30.69-31.71 Å: dashed line) and W^{26+} (29.47-30.47 : dotted line) calculated with (b) the present CR model and (c) ADAS code.

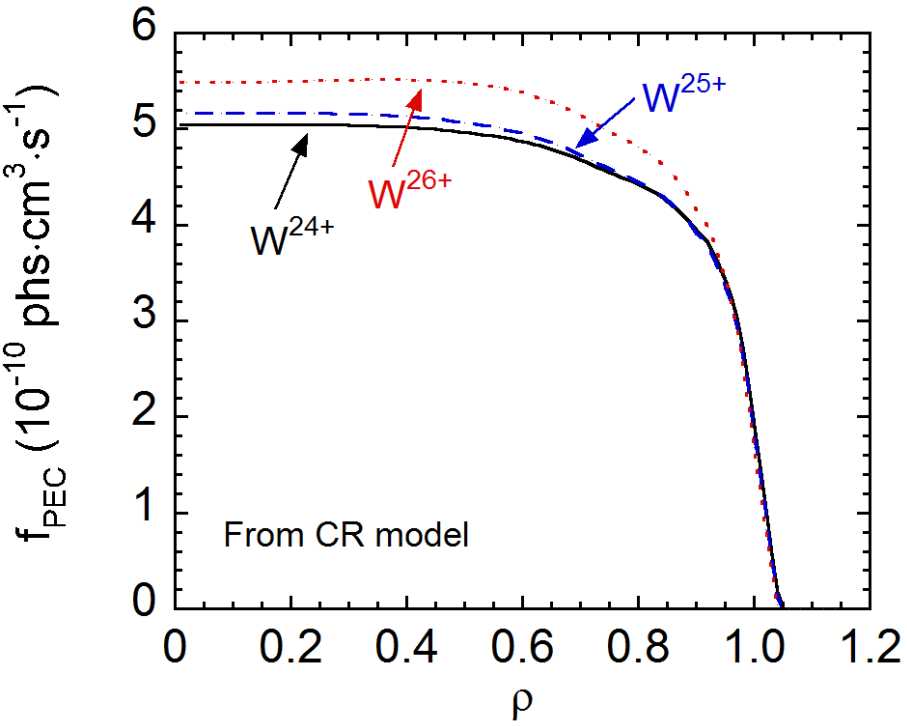

Fig. 6. Photon emission coefficients of W^{24+} (32.16-33.32 Å), W^{25+} (30.69-31.71 Å) and W^{26+} (29.47-30.47 Å) from the present CR model against normalized radius at t = 4.7 s in Fig.2.

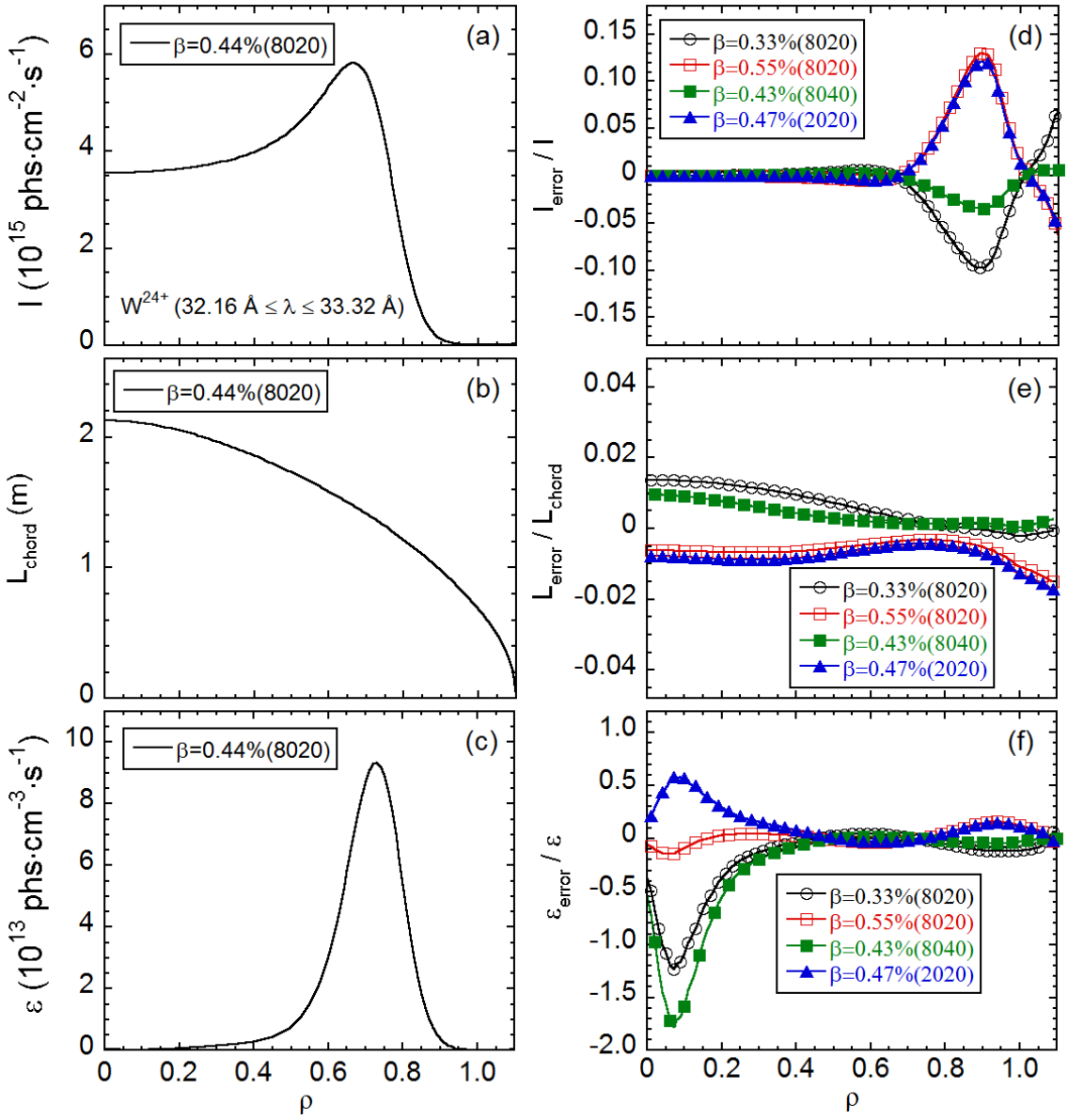

Fig. 7. (a) Line-integrated vertical intensity at 32.16-33.32 Å taken at Δt = 0.3 s after tungsten pellet (tungsten wire: 0.05 mm^{ϕ} × 1.0 mm^{L}) injection, (b) observation chord length, (c) local emissivity after Abel inversion for β = 0.44% (8020) at R_{ax} = 3.60 m, and normalized errors of (d) line-integrated vertical intensity, I_{error}/I, (e) observation chord length, L_{error}/L_{chord} and (f) local emissivity, $\varepsilon_{error}/\varepsilon$ for different β and pressure profiles. The vertical position in the vertical intensity profile of Fig. 7(a) is converted into the normalized radius. Notation of "β = 0.44% (8020)" means pressure profile of $P(\rho)=P_0(1-\rho^8)(1-\rho^2)$ with volume-averaged beta of 0.44%, where P_0 is central pressure.

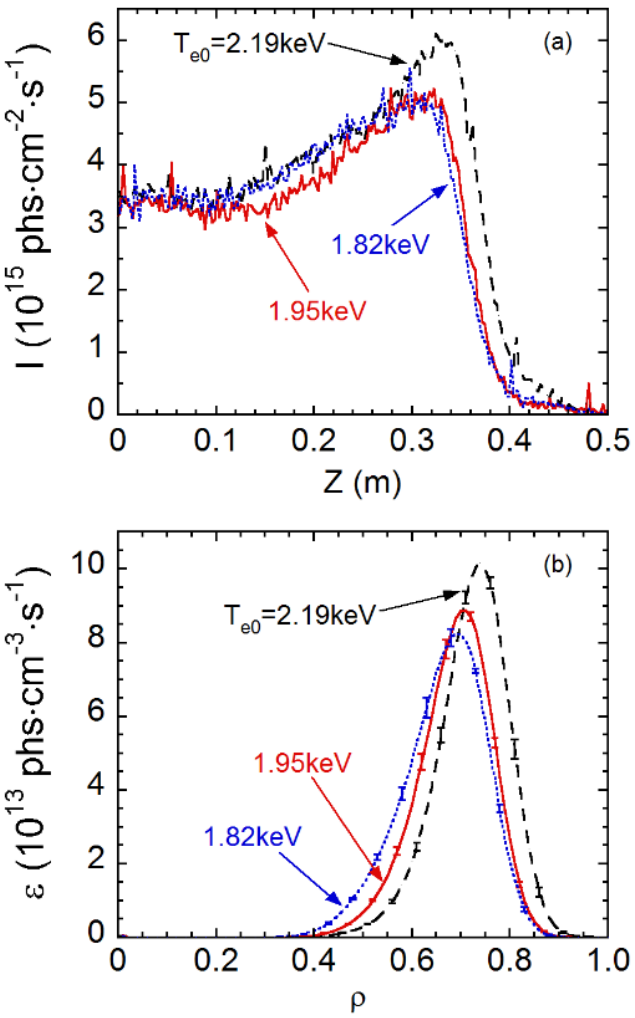

Fig. 8. (a) Vertical intensity and (b) local emissivity profiles of W^{24+} at wavelength interval of 32.16-33.32 Å plotted at different central electron temperatures of T_{e0} = 2.19 (dashed line), 1.95 (solid line) and 1.82 keV (dotted line).

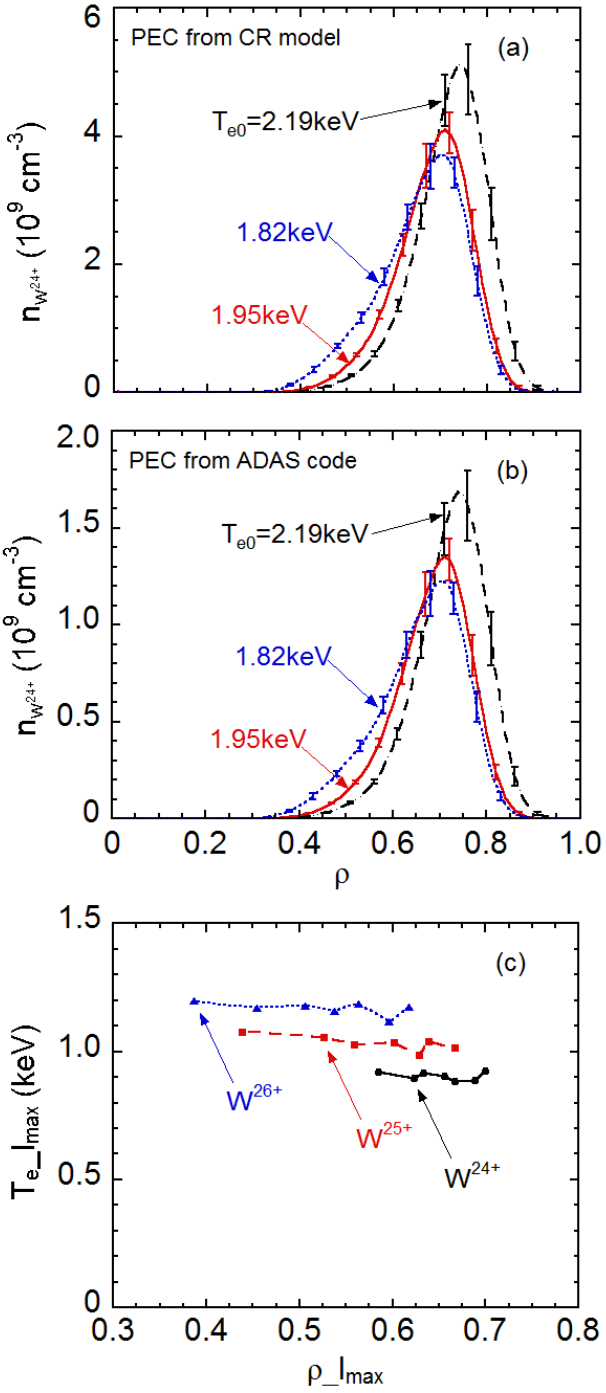

Fig. 9. Density profiles of W^{24+} ions at T_{e0} = 2.19 (dashed line), 1.95 (solid line) and 1.82 keV (dotted line) using photon emission coefficient calculated with (a) the present CR model and (b) ADAS code. (c) Electron temperature where the vertical intensity profile of W^{24+} (32.16-33.32 Å), W^{25+} (30.69-31.71 Å) and W^{26+} (29.47-30.47 Å) takes the maximum value as a function of normalized radius at the intensity maximum.

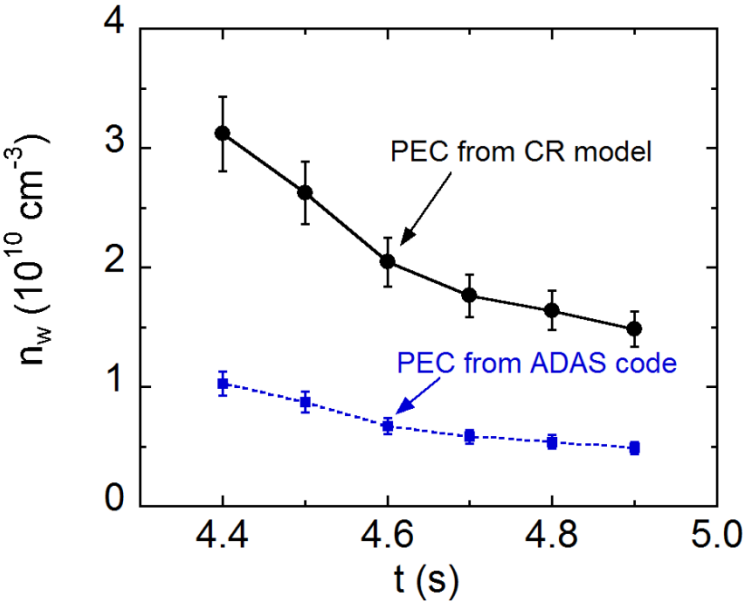

Fig. 10. Time trace of total tungsten density in the vicinity of $\rho = 0.7$ calculated at peak value of W^{24+} ion density profile (solid circles: the present CR model, solid squares: ADAS code).

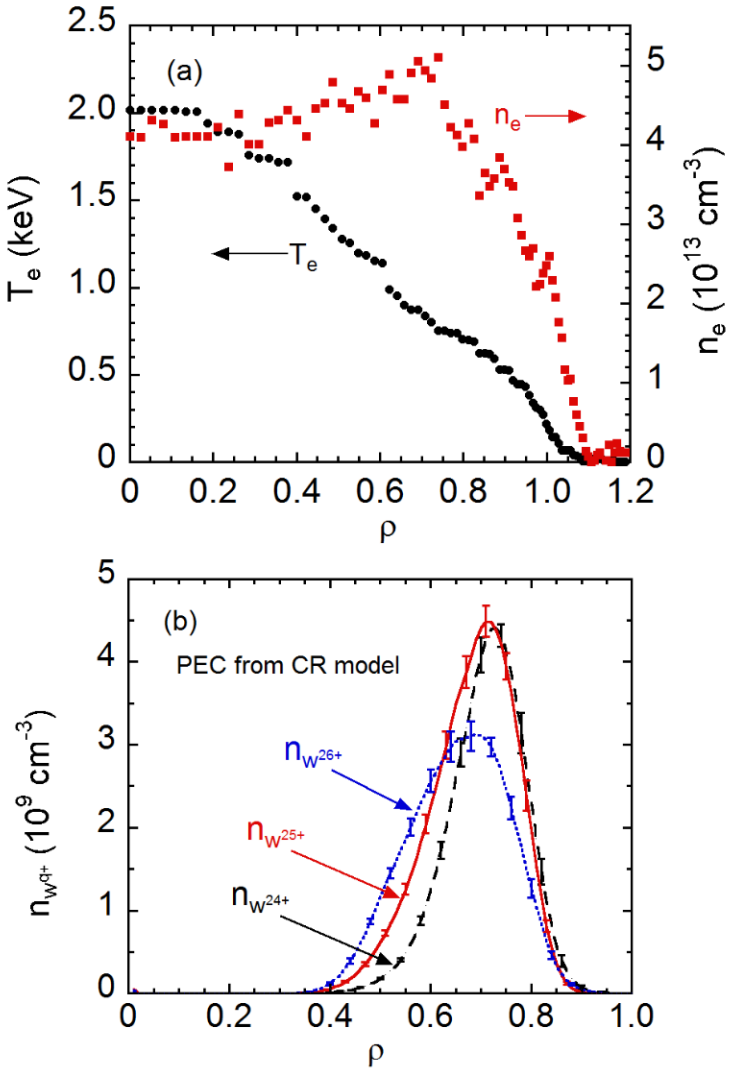

Fig. 11. (a) Electron density (solid squares) and temperature (solid circles) profiles and (b) tungsten density profiles of W^{24+} (dashed line), W^{25+} (solid line) and W^{26+} (dotted line) ions at t = 4.7 s in Fig.2.

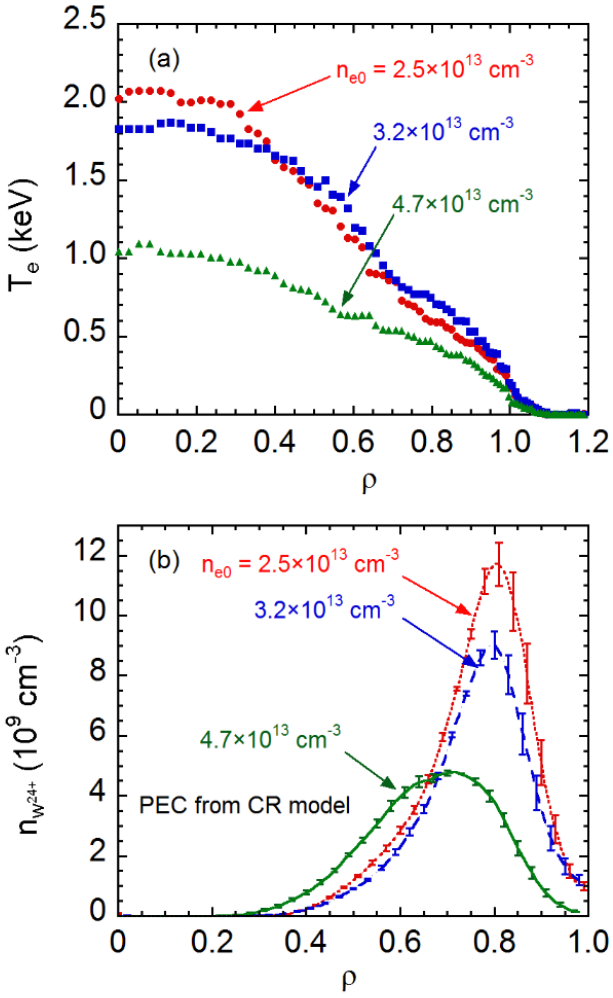

Fig. 12. (a) Electron temperature and (b) W^{24+} ion density profiles at Δt = 0.1 s after pellet injection (0.06 mm^{ϕ} × 1.0 mm^{L}) in different electron densities of 2.5 × 10^{13} cm^{-3} (dotted line), 3.2 × 10^{13} cm^{-3} (dashed line) and 4.7 × 10^{13} cm^{-3} (solid line).

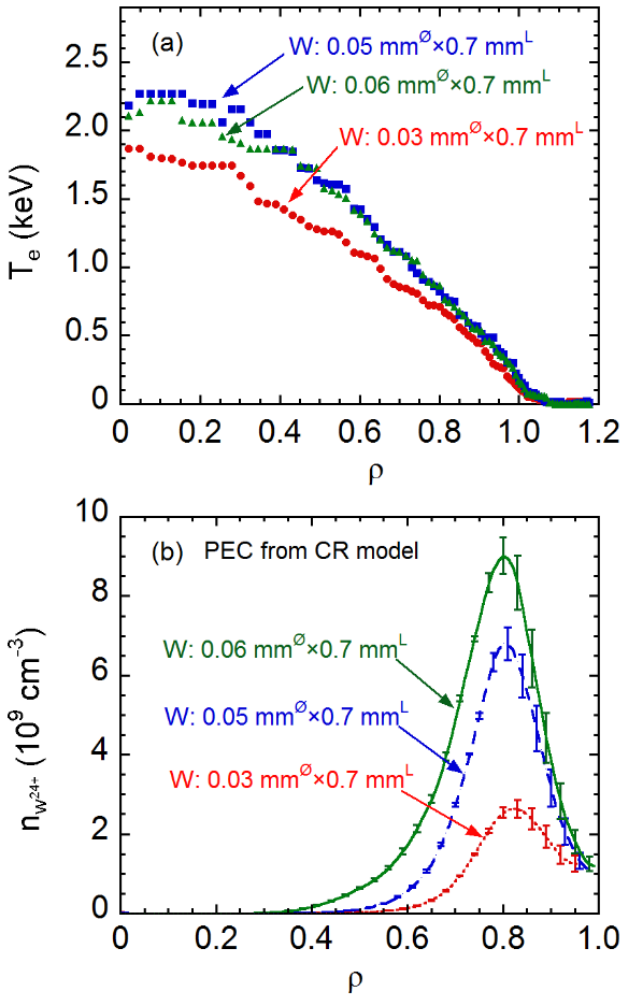

Fig. 13. (a) Electron temperature and (b) W^{24+} ion density profiles at Δt = 0.1 s after pellet injection with different tungsten pellet seizes of 0.03 mm$^{\phi}$ × 1.0 mm^{L} (dotted line), 0.05 mm$^{\phi}$ × 1.0 mm^{L} (dashed line) and 0.06 mm$^{\phi}$ × 1.0 mm^{L} (solid line).